Journal of the Mechanics and Physics of Solids ▮ (▮▮▮▮) ▮▮▮–▮▮▮

Contents lists available at ScienceDirect

Journal of the Mechanics and Physics of Solids

journal homepage: www.elsevier.com/locate/jmps

Non linear constitutive models for lattice materials

Andrea Vigliotti [a], Vikram S. Deshpande [b], Damiano Pasini [a,*]

[a] Department of Mechanical Engineering, McGill University, 845 Sherbrooke St. W, Montreal H3A 2T5, Canada
[b] Department of Engineering, University of Cambridge, Trumpington Street, Cambridge CB2 1PZ, UK

ARTICLE INFO

Article history:
Received 19 December 2012
Received in revised form
15 October 2013
Accepted 27 October 2013

Keywords:
Lattice materials
Periodic cellular materials
Multiscale mechanics
Non linear mechanics

ABSTRACT

We use a computational homogenisation approach to derive a non linear constitutive model for lattice materials. A representative volume element (RVE) of the lattice is modelled by means of discrete structural elements, and macroscopic stress–strain relationships are numerically evaluated after applying appropriate periodic boundary conditions to the RVE. The influence of the choice of the RVE on the predictions of the model is discussed. The model has been used for the analysis of the hexagonal and the triangulated lattices subjected to large strains. The fidelity of the model has been demonstrated by analysing a plate with a central hole under prescribed in plane compressive and tensile loads, and then comparing the results from the discrete and the homogenised models.

1. Introduction

Lattice materials are a class of cellular materials characterised by a regular, periodic microstructure that can be idealised as a network of slender beams or rods. As all cellular materials, they combine properties such as lightness, stiffness, strength and high energy absorbing capabilities that cannot be achieved by uniform fully solid materials (Ashby, 2005; Fleck et al., 2010; Gibson and Ashby, 1999; Banhart, 2001). In addition, due to their regular and controlled microstructure, lattice materials can be designed to fulfil specific requirements, such as prescribed stiffness and strength along given directions and predetermined collapse modes.

Recent advances in manufacturing techniques allow the production of lattice materials from a variety of solid materials, at a very fine scale, with high accuracy and within acceptable costs (Bidanda and Bartolo, 2008; Ramirez et al., 2011; Schaedler et al., 2011). Such technologies make lattice materials a viable option for use in the design of consumer products, and have driven the interest in modelling tools for the analysis of complex components made of lattice materials. Applications that exploit the design of bending dominated lattices for morphing structures, and that focus on stretching dominated lattices suitable for reconfigurable and smart actuated structures (Fleck et al., 2010; Wang et al., 2007; Spadoni and Ruzzene, 2007) typically require modelling lattice materials into the non linear regime. However, the literature on the modelling of the mechanical properties of lattice materials is generally restricted to the geometrically linear regime.

In this paper, we are concerned with the derivation of a constitutive model for the analysis of the geometrically non linear behaviour of lattices. A number of studies have analysed simple topologies and obtained closed-form expressions of the lattice stiffness and strength by solving the equilibrium problem of the unit cell (Gibson and Ashby, 1982; Wang and McDowell, 2004; Gibson et al., 1982; Zhu et al., 1997; Hutchinson and Fleck, 2006). This approach cannot in general be

* Corresponding author. Tel.: +1 514 398 6895; fax: +1 514 398 7365.
E-mail address: damiano.pasini@mcgill.ca (D. Pasini).

0022-5096/$ - see front matter © 2013 Elsevier Ltd. All rights reserved.
http://dx.doi.org/10.1016/j.jmps.2013.10.015

extended to include geometrical non linearities, because closed-form solutions are typically unavailable for a beam under large displacement. In other homogenisation approaches (Kumar and McDowell, 2004; Langley, 1996; Suiker et al., 2001; Gonella and Ruzzene, 2008; Elsayed and Pasini, 2010a,b; Vigliotti and Pasini, 2012a,b), the equivalent stiffness of the lattice is determined by comparing selected physical quantities of the discrete lattice, such as the dispersion relation of harmonic waves, or the coefficients of the elastic equilibrium equation, to those of an equivalent continuous medium. These models are necessarily restricted to the linear regime and cannot be extended to consider the effects of geometric or material non linearity. Despite the lack of a specific literature on non linear models for lattices, several works, mainly focused on the modelling of composites and of heterogeneous media, are available. These studies can offer insight into the general framework and theoretical basis for the development of a non linear constitutive model for lattices. Extensive reviews of these works have been produced by Pindera et al. (2009), and by Charalambakis (2010).

The approach presented in this study belongs to the class of representative volume element (RVE) methods (Kouznetsova et al., 2001, 2002, 2004; Van Der Sluis et al., 2000; Terada et al., 2000; Smit et al., 1998; Matsui et al., 2004; Fish and Wagiman, 1993; Mohr, 2005; Ohno et al., 2002), which evaluate the constitutive relationships of a heterogeneous medium from the analysis of a small portion of it. The RVE consists in a limited region of the domain that contains the main microstructural features of the material and responds as the infinite medium, if uniform strain, or stress, and boundary conditions are imposed. All these methods are based on the self-consistent scheme developed by Eshelby (1957), who studied the mechanics of an ellipsoidal inclusion in an infinite matrix with homogeneous boundary conditions. In general, RVE methods resort to a two-scale approach. On one hand, there is the macroscopic finite element model of the component, whose boundary conditions are defined by the general problem, where the material is treated as a homogeneous continuum. On the other hand, there exists the microscopic model of the RVE, which numerically evaluates the stress–strain relationship, whose boundary conditions are generated by the macroscopic model. The RVE model is interrogated at every integration point of the component model, a process that allows the assembly of the macroscopic internal force vector and of the tangent stiffness matrix, as it is done for a fully solid material. These methods, developed for random media, where the RVE is modelled by means of continuous elements, evaluate the macroscopic stress as the average of the microscopic stress on the RVE. Such techniques while feasible for lattice materials (Kouznetsova et al., 2001, 2002, 2004; Van Der Sluis et al., 2000; Ohno et al., 2002) are numerically very cumbersome. It is more natural for these materials to consider RVEs with discrete structural elements, such as beams or shells. However, we typically do not want to carry higher order stresses, such as moments, from the micro- to the macro-scales. For instance, we could not evaluate the contribution to the macroscopic stress of the lattice of a single beam in pure bending, because the stress average over the cross section would be null everywhere along the beam, even though a lattice comprising such elements will sustain a finite macroscopic stress. Other works (Kumar and McDowell, 2004) derive macroscopic constitutive relations for trusses assuming a homogeneous displacement model for the RVE. Such an approach is valid for RVEs that hold central symmetry; nevertheless, if the RVE loses its symmetry during loading, as a consequence of large macroscopic strain, or post-bifurcation, the displacement field of the RVE cannot be described as homogeneous and it should be determined enforcing the equilibrium.

In this study, we use an alternative approach, which allows us to determine the macroscopic stress as the gradient of the strain energy density with respect to the components of the macroscopic displacement gradient. This formulation leads to a compact matrix expression for the macroscopic stress as a function of the macroscopic displacement gradient that can handle both geometrical and material non linearities. The kinematic assumption undertaken here is that the deformation of the lattice periodic directions is congruent with the macroscopic displacement gradient, while the RVE configuration is determined by imposing periodic equilibrium conditions on the RVE. As with any RVE approach, the analysis presented here also assumes periodic deformations and thus cannot account for random spatially distributed imperfections within the lattice material.

The choice of the RVE plays an important role in the framework of a computational homogenisation approach (Gusev, 1997; Kanit et al., 2003; Gitman et al., 2007; Terada et al., 2000; Graham and Yang, 2003; Stroeven et al., 2004). Most of these studies focus on materials with a stochastic microstructure, and are aimed at determining the conditions that ensure a statistical representativeness of the RVE, both for the purpose of numerical homogenisation and for the definition of the size, shape, and number of samples required for experimentally measuring the material properties. Since our focus is on periodic lattices, a natural choice for the RVE is the unit cell, which we intend as the minimal entity capable of generating the lattice. Such choice, however, is not unique; any collection of contiguous unit cells can be used as RVE. Hence, the following question arises: how does the size of the RVE affect the response of the material? For example, Braides (1985) and Müller (1987) have shown that one should not generally expect a finite RVE in the context of finite deformation and that bifurcations can occur at any length scale. Triantafyllidis and Schraad (1998) and Gong et al. (2005) have taken these works ahead by showing explicitly, using Bloch wave boundary conditions, that some bifurcations occur only as the RVE size goes to infinity. This paper addresses this issue of RVE size choice with particular reference to the effect of geometric non linearity. We show that the size of the RVE has no influence on the model prediction, until a bifurcation point is encountered in the load path. After passing bifurcations, the predicted post-bifurcation behaviour depends on the size of the RVE; hence, preliminary investigations should be carried out for a proper selection of the RVE.

The constitutive material model presented in this paper is validated by comparing the results of a discrete and a continuous model of a rectangular plate with a central hole under in-plane loads. In one case, a direct numerical simulation has been carried out on the discrete lattice, whose elements have been individually modelled as beams. In the other case, the domain was modelled with continuous plane stress elements whose constitutive law was numerically evaluated using the homogenisation approach developed in this study.

Please cite this article as: Vigliotti, A., et al., Non linear constitutive models for lattice materials. J. Mech. Phys. Solids (2013), http://dx.doi.org/10.1016/j.jmps.2013.10.015

2. Description of the methodology

Given a lattice material comprising a periodic array of connected struts or beams, a direct numerical simulation would involve performing structural calculations in which every strut of the lattice material is modelled individually. This is however very computationally expensive, even for a very simple geometry. In this study, we derive a non linear numerical constitutive model for lattices that allows the modelling of components made of lattice material using a continuum description, wherein every strut of the underlying lattice is not explicitly modelled. Fig. 1 illustrates the multiscale scheme for the derivation of the macroscopic stress by means of a finite element model of a representative volume element of the lattice. At every integration point of the macroscopic model, the first Piola–Kirchoff tensor, **P**, is evaluated by means of a finite element model of the RVE. The macroscopic displacement gradient, **G**, defines the variation of the periodic directions of the lattice, and introduces the boundary conditions for the microscopic model. Once the microscopic boundary value problem (b.v.p.) is solved and the equilibrium configuration of the RVE has been found, we can determine the components of **P** as the derivatives of the strain energy density of the lattice with respect to **G**. We emphasise here that the microscopic problem contains higher order stresses (moments) as the struts of the lattice are modelled as beams. However, these moments are not explicitly retained as we move from the macro- to micro-scale with only **P** and **G**, used to describe the state at the macro-scale. This homogenisation is done consistently via the principle of virtual work as shall be described subsequently.

Let **s** be the array of the nodal degrees of freedom of the RVE, the corresponding array of the nodal forces, **F**(**s**), can be calculated by a Finite Element (FE) analysis of the RVE. The first order variation of the strain energy, due to a variation of the macroscopic strain, can then be obtained by applying the principle of the virtual work as follows:

$$\mathrm{d}W = \int_{V_{RVE}} P_{ij}\,\mathrm{d}G_{ij}\,\mathrm{d}V = \mathbf{F}^T\,\mathrm{d}\mathbf{s} \tag{1}$$

where: P_{ij} and G_{ij} are respectively the components of the macroscopic first Piola–Kirchoff (1PK) stress tensor and of the macroscopic displacement gradient; d**s** is the variation of the nodal displacements corresponding to dG_{ij}. Assuming that P_{ij} and G_{ij} are uniform over the RVE, we obtain the following expression for the macroscopic stress tensor

$$P_{ij} = \frac{1}{V_{RVE}}\frac{\partial W}{\partial G_{ij}} = \frac{1}{V_{RVE}}\mathbf{F}^T\frac{\partial \mathbf{s}}{\partial G_{ij}} \tag{2}$$

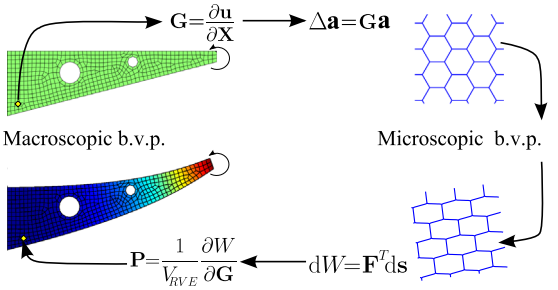

Fig. 1. Multiscale scheme. At each integration point of the macroscopic model the constitutive relations are found by solving a boundary value problem (b.v.p.) on a RVE of the lattice.

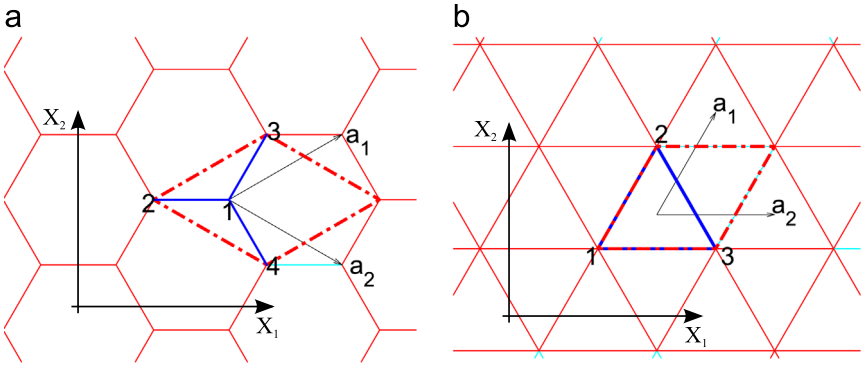

Fig. 2. Sample lattice topologies. Thick blue lines represent the unit cell elements; dashed red lines describe RVE boundaries while $\mathbf{a}_1$ and $\mathbf{a}_2$ are the tessellation vectors. $\mathbf{X}_1$ and $\mathbf{X}_2$ are the coordinate directions of the Cartesian reference system. (a) Hexagonal lattice, (b) triangular lattice. (For interpretation of the references to colour in this figure caption, the reader is referred to the web version of this article.)

Please cite this article as: Vigliotti, A., et al., Non linear constitutive models for lattice materials. J. Mech. Phys. Solids (2013), http://dx.doi.org/10.1016/j.jmps.2013.10.015

To calculate the derivatives on the right hand side of Eq. (2), we introduce the following kinematic assumptions:

(i) the periodic directions of the lattice change according to the macroscopic displacement gradient;
(ii) the lattice remains periodic during deformation.

We remark that assumption (i) applies only to the periodic directions; no further restrictive hypothesis is made on the displacement of the internal points of the RVE, whose configuration is determined by imposing the equilibrium. We also note that the above assumptions are equivalent to considering that the size of the RVE is negligible with respect to the size of the macroscopic domain, and that the typical length of the lattice elements is negligible with respect to the local wavelength of the macroscopic strain field. In other words, the RVE is considered as a material point of the macroscopic continuum; hence in this formulation, the macroscopic and the microscopic length scales are completely decoupled.

To determine the array $\partial \mathbf{s}/\partial G_{ji}$, consider, as an example, the lattices in Fig. 2. In this section, for the sake of simplicity, we consider RVEs that contain a single Unit Cell (UC).[1] As we can note, all the boundary nodes of the RVE are necessarily positioned along the periodic vectors, $\mathbf{a}_1$ and $\mathbf{a}_2$, while the position of the internal nodes cannot be written in terms of other nodes in the RVE via $\mathbf{a}_i$. For instance, in Fig. 2a the position $\mathbf{r}_3$ of node 3 can be written in terms of $\mathbf{r}_2$ as $\mathbf{r}_3=\mathbf{r}_2+\mathbf{a}_1$, while the position of node 4 in terms of the position of node 2 is $\mathbf{r}_4=\mathbf{r}_2+\mathbf{a}_2$; in the same figure, node 1 is internal and has no corresponding node along any periodic direction in the RVE. Similarly in Fig. 2b, the position of node 2 in terms of node 1 is written as $\mathbf{r}_2=\mathbf{r}_1+\mathbf{a}_1$, while the position of node 3 is given as $\mathbf{r}_3=\mathbf{r}_1+\mathbf{a}_2$, and in this case we do not have an internal node. It follows that we can express the position of all the nodes of the unit cell by means of the position of the independent nodes as

$$\mathbf{r}_i=\overline{\mathbf{r}}_j+k\mathbf{a}_1+h\mathbf{a}_2 \tag{3}$$

where $\overline{\mathbf{r}}_j$ are the positions of the independent nodes with $k,h\in -1,0,1$ (for internal nodes $k=h=0$), $j\in 1\ldots\overline{N}$, with $\overline{N}$ being the number of independent nodes of the RVE, and $i\in 1\ldots N$, where N are the number of the dependent nodes of the RVE. The displacement $\mathbf{s}_i$ of the ith dependent node is written in terms of the displacement $\overline{\mathbf{s}}_j$ of the independent nodes as

$$\mathbf{s}_i=\overline{\mathbf{s}}_j+k\Delta\mathbf{a}_1+h\Delta\mathbf{a}_2 \tag{4}$$

where $\Delta\mathbf{a}_i$ is the change in the ith tessellation direction. Collecting all the DoFs of the UC in the array $\mathbf{s}$ allows writing the following equation in a compact matrix form as

$$\mathbf{s}=\mathbf{B}_0\overline{\mathbf{s}}+\mathbf{B}_1\Delta\mathbf{a} \tag{5}$$

where the entries of the matrices $\mathbf{B}_0$ and $\mathbf{B}_1$ are $1,0$ or -1, and do not change during the deformation; $\overline{\mathbf{s}}$ is the array that collects all the independent degrees of freedom (DoF) of the unit cell, while $\Delta\mathbf{a}$ groups the components of $\Delta\mathbf{a}_i$ and is defined as

$$\Delta\mathbf{a}=[\Delta a_{11},\ \Delta a_{12},\ \Delta a_{21},\ \Delta a_{22}]^T \tag{6}$$

where the first index refers to the periodic direction, and the second index to the Cartesian component. If $G_{ij}=\partial u_i/\partial X_j$ are the components of the macroscopic displacement gradient, the following holds

$$\Delta a_{ki}=G_{ij}a_{kj} \tag{7}$$

After collecting the components of the gradient in the array $\mathbf{G}=[G_{11},\ G_{12},\ G_{21},\ G_{22}]^T$, we can express the change in the periodic directions as a function of the components of the displacement gradient as

$$\Delta\mathbf{a}=\mathbf{B}_\mathbf{a}\mathbf{G} \tag{8}$$

where the matrix $\mathbf{B}_\mathbf{a}$ gathers the components of the tessellation vectors rearranged as

$$\mathbf{B}_\mathbf{a}=\begin{bmatrix} a_{11} & a_{12} & 0 & 0\\ 0 & 0 & a_{11} & a_{12}\\ a_{21} & a_{22} & 0 & 0\\ 0 & 0 & a_{21} & a_{22}\end{bmatrix} \tag{9}$$

Hence, all the DoFs of RVE can be directly expressed as a function of the DoFs of the independent nodes and of the components of the displacement gradient as

$$\mathbf{s}=\mathbf{B}_0\overline{\mathbf{s}}+\mathbf{B}_G\mathbf{G} \tag{10}$$

where $\mathbf{B}_G=\mathbf{B}_1\mathbf{B}_a$ and depends on the topology of the RVE only. Eq. (10) expresses the kinematics of the RVE, and relates the macroscopic displacement gradient $\mathbf{G}$ to the nodal displacements of the RVE. We remark that the deformed shape of the RVE can be found after the DoFs of the independent nodes, $\overline{\mathbf{s}}$, have been determined; this can be done by enforcing the periodic equilibrium condition on the RVE.

[1] The effect of RVE size is considered in detail in Sections 2.1 and 3.

Please cite this article as: Vigliotti, A., et al., Non linear constitutive models for lattice materials. J. Mech. Phys. Solids (2013), http://dx.doi.org/10.1016/j.jmps.2013.10.015

Thanks to assumption (ii), we can write the equation for the equilibrium of the RVE, under the action of the surrounding elements, in terms of the nodal forces of the same RVE. In particular, the following holds for the hexagonal lattice

$$\begin{aligned}&\mathbf{F}_1=\mathbf{0}\\&\mathbf{F}_2+\mathbf{F}_3+\mathbf{F}_4=\mathbf{0}\end{aligned}\tag{11}$$

where the subscript refers to the nodes numbers as marked in Fig. 2. Similarly for the triangulated lattice, we can write the following periodic equilibrium equation

$$\mathbf{F}_1+\mathbf{F}_2+\mathbf{F}_3=\mathbf{0}\tag{12}$$

It is possible to show (Vigliotti and Pasini, 2012a) that for an arbitrary lattice the periodic equilibrium equation can be written in terms of the $\mathbf{B}_0$ matrix as

$$\mathbf{B}_0^T\mathbf{F}(\mathbf{s})=0\tag{13}$$

and by means of Eq. (10) as follows:

$$\mathbf{B}_0^T\mathbf{F}(\mathbf{B}_0\overline{\mathbf{s}}+\mathbf{B}_G\mathbf{G})=0\tag{14}$$

The above equation expresses the equilibrium of the unit RVE under the action of the surrounding cells, for a uniform deformation field. Given $\mathbf{G}$, Eq. (14) can be solved using a Newton Raphson scheme, i.e. updating the nodal DOFs $\overline{\mathbf{s}}^i$ of the independent nodes after the ith iteration via

$$\mathbf{R}^i=\mathbf{B}_0^T\mathbf{F}(\mathbf{B}_0\overline{\mathbf{s}}^i+\mathbf{B}_G\mathbf{G})\tag{15}$$

$$\overline{\mathbf{s}}^{i+1}=\overline{\mathbf{s}}^i-\left(\frac{\partial\mathbf{R}}{\partial\overline{\mathbf{s}}}\right)^{-1}\mathbf{R}^i\tag{16}$$

where $\mathbf{R}^i$ is the residual after the iteration i and $\partial\mathbf{R}/\partial\overline{\mathbf{s}}=\mathbf{B}_0^T(\partial\mathbf{F}/\partial\mathbf{s})\mathbf{B}_0$. It now remains to calculate the macroscopic 1PK tensor by means of Eq. (2). To determine $\partial\mathbf{s}/\partial G_{ij}$, we differentiate Eq. (10) with respect to $\mathbf{G}$ to obtain:

$$\frac{\partial\mathbf{s}}{\partial\mathbf{G}}=\mathbf{B}_0\frac{\partial\overline{\mathbf{s}}}{\partial\mathbf{G}}+\mathbf{B}_G\tag{17}$$

and thereby the components of the 1PK tensor, collected in the array $\mathbf{P}$, are

$$\mathbf{P}=\frac{1}{V_{RVE}}\mathbf{F}^T\left(\mathbf{B}_0\frac{\partial\overline{\mathbf{s}}}{\partial\mathbf{G}}+\mathbf{B}_G\right)\tag{18}$$

This is further simplified by employing Eq. (13) to give

$$\mathbf{P}=\frac{1}{V_{RVE}}\mathbf{B}_G^T\mathbf{F}(\mathbf{s})\tag{19}$$

We now proceed to determine the solution to the macroscopic problem. To do this we need to calculate the Jacobian of the stress tensor with respect to the displacement gradient, i.e. $\partial\mathbf{P}/\partial\mathbf{G}$. Differentiating Eq. (18) with respect to $\mathbf{G}$ allows writing:

$$\frac{\partial\mathbf{P}}{\partial\mathbf{G}}=\frac{1}{V_{RVE}}\left[\left(\frac{\partial\mathbf{F}}{\partial\mathbf{s}}\frac{\partial\mathbf{s}}{\partial\mathbf{G}}\right)^T\left(\mathbf{B}_0\frac{\partial\overline{\mathbf{s}}}{\partial\mathbf{G}}+\mathbf{B}_G\right)+\mathbf{F}^T\mathbf{B}_0\frac{\partial^2\overline{\mathbf{s}}}{\partial\mathbf{G}^2}\right]\tag{20}$$

where $\partial\mathbf{F}/\partial\mathbf{s}$ is the tangent stiffness matrix of the unconstrained RVE, and $\partial\mathbf{s}/\partial\mathbf{G}$ is given by Eq. (17). Eq. (13) implies that the term with $\partial^2\overline{\mathbf{s}}/\partial\mathbf{G}^2$ in Eq. (20) vanishes and using the symmetry of $\partial\mathbf{F}/\partial\mathbf{s}$, we obtain

$$\frac{\partial\mathbf{P}}{\partial\mathbf{G}}=\frac{1}{V_{RVE}}\left(\mathbf{B}_0\frac{\partial\overline{\mathbf{s}}}{\partial\mathbf{G}}+\mathbf{B}_G\right)^T\frac{\partial\mathbf{F}}{\partial\mathbf{s}}\left(\mathbf{B}_0\frac{\partial\overline{\mathbf{s}}}{\partial\mathbf{G}}+\mathbf{B}_G\right)\tag{21}$$

It now remains to calculate $\partial\overline{\mathbf{s}}/\partial\mathbf{G}$ which represents the first variation of the internal DoFs of the RVE corresponding to a variation in G. Since $\overline{\mathbf{s}}$ has to satisfy the RVE equilibrium always, $\partial\overline{\mathbf{s}}/\partial\mathbf{G}$ can be found by differentiating Eq. (13) with respect to $\mathbf{G}$, and recalling (17), which yields

$$\mathbf{B}_0^T\frac{\partial\mathbf{F}}{\partial\mathbf{s}\,\frac{\partial\mathbf{s}}{\partial\mathbf{G}}}=\mathbf{B}_0^T\frac{\partial\mathbf{F}}{\partial\mathbf{s}}\left(\mathbf{B}_0\frac{\partial\overline{\mathbf{s}}}{\partial\mathbf{G}}+\mathbf{B}_G\right)=0\tag{22}$$

We can calculate $\partial\overline{\mathbf{s}}/\partial\mathbf{G}$ by solving

$$\left(\mathbf{B}_0^T\frac{\partial\mathbf{F}}{\partial\mathbf{s}}\mathbf{B}_0\right)\frac{\partial\overline{\mathbf{s}}}{\partial\mathbf{G}}=-\mathbf{B}_0^T\frac{\partial\mathbf{F}}{\partial\mathbf{s}}\mathbf{B}_G.\tag{23}$$

We observe that the matrix $\mathbf{B}_0^T(\partial\mathbf{F}/\partial\mathbf{s})\mathbf{B}_0$ is square but not invertible. Yet, since both the terms in Eq. (23) belong to the column range of $\mathbf{B}_0^T$, a solution must always exist and is given by

$$\frac{\partial\overline{\mathbf{s}}}{\partial\mathbf{G}}=-\left(\mathbf{B}_0^T\frac{\partial\mathbf{F}}{\partial\mathbf{s}}\mathbf{B}_0\right)^+\mathbf{B}_0^T\frac{\partial\mathbf{F}}{\partial\mathbf{s}}\mathbf{B}_G\tag{24}$$

Please cite this article as: Vigliotti, A., et al., Non linear constitutive models for lattice materials. J. Mech. Phys. Solids (2013), http://dx.doi.org/10.1016/j.jmps.2013.10.015

where $()^+$ denotes the Moore–Penrose pseudo inverse. Eq. (24), substituted in Eq. (21), yields the numerical expression for the sought Jacobian.

Through Eqs. (19) and (21), we can evaluate the 1PK tensor and its Jacobian for any given **G**, and solve the equilibrium problem of a macroscopic component made of lattice material by means of standard displacement-based finite element procedures. We observe that the boundary conditions for the RVE problem are produced during the iterations at the macro level; therefore, a robust algorithm capable of handling instabilities and snap-through of the RVE is necessary to solve Eqs. (14). The algorithm should be able to automatically detect if a bifurcation point has already been crossed, or if a bifurcation is close to the current equilibrium point, and perform branch switching to bring the structure in the lowest potential energy configuration. The method described by Crisfield (1981, 1998) meets these criteria and was thus used to generate the results presented here. At the beginning of each increment, the eigenvector of $\partial\mathbf{R}/\partial\overline{\mathbf{s}}$ corresponding to the lowest eigenvalue is extracted, and a line search along this eigenvector is performed to minimise the norm of **P**; subsequently, this point is used as initial guess for the local iterations. A combination of Newton Raphson and Riks steps is performed in proximity of the bifurcation points to improve convergence. The technique proved to be satisfactorily robust and was able to detect the occurrence of buckling and deviation from the equilibrium path on low energy branches.

In the formulation presented in this paper, all boundary conditions are on the components of **G**, which ensures the existence of a solution. It is also possible to pose the inverse problem, that is to consider boundary conditions given on the **P** tensor and solve for **G**. Yet in this case, the existence of the solution is not guaranteed due to the existence of limit loads for the RVE. We can alternatively consider mixed boundary conditions, where certain components of **P** and **G** are prescribed and others are free. Nevertheless, since the components of **G** and **P** are directly work conjugated, the same component cannot be prescribed on both tensors.

3. Effect of the RVE size

A key element of a homogenisation approach is the choice of the RVE. Given the unit cell of the lattice and the periodic directions, alternative RVEs can be generated including more unit cells along the periodic directions. Fig. 3 shows four different choices including 2, 3, 5, and 7 UC along each periodic direction. It is critical to understand how a particular choice of the RVE might influence the predicted equilibrium configuration of the lattice.

We start by showing that until a bifurcation is encountered on the load path of the lattice, the predictions of the model are independent from the RVE. To illustrate this, we refer to Fig. 4; let RVE^{ij} be four contiguous identical RVEs as labelled in Fig. 4 while l^{ij}, b^{ij}, r^{ij} t^{ij} refer to the left, bottom, right and top boundaries, respectively of RVE^{ij}. Consider first RVE^{11} for a given macroscopic displacement gradient **G** acting on the lattice. We can solve (14) to find the configuration of the independent

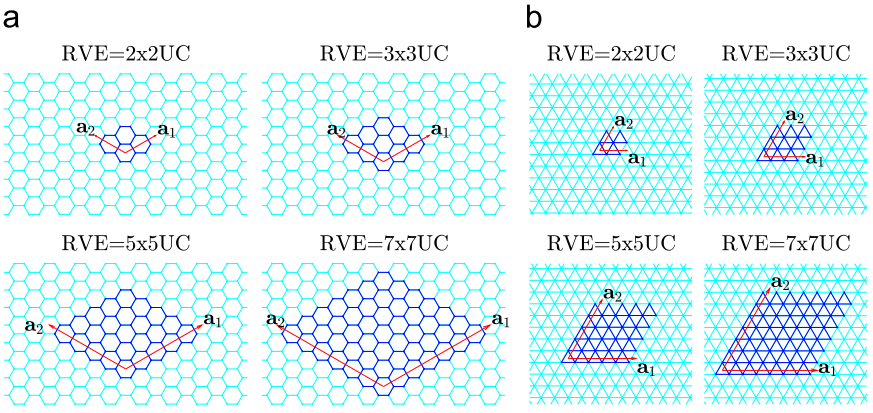

Fig. 3. Some selected RVE sizes considered in this study. (a) Hexagonal lattice, (b) triangular lattice.

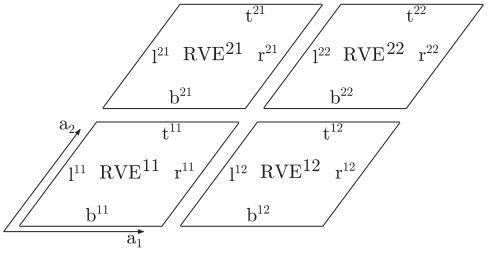

Fig. 4. Notation used to define four identical RVEs, RVE^{ij}, and their boundary segments l^{ij}, b^{ij}, r^{ij}, t^{ij}.

Please cite this article as: Vigliotti, A., et al., Non linear constitutive models for lattice materials. J. Mech. Phys. Solids (2013), http://dx.doi.org/10.1016/j.jmps.2013.10.015

DoFs of the RVE, $\bar{\mathbf{s}}^{11}$; then by means of equation (10), we determine all the DoF, $\mathbf{s}^{11}$, and the nodal forces, $\mathbf{F}^{11}$, of RVE^{11}, which in turn yields $\mathbf{P}$. The compatibility conditions for the boundary nodes, Eq. (4), and the periodic equilibrium conditions yield the following

$$\begin{aligned} &\mathbf{s}_r^{11}-\mathbf{s}_l^{11}=\Delta\mathbf{a}_1, \quad \mathbf{F}_l^{11}+\mathbf{F}_r^{11}=\mathbf{0}\\ &\mathbf{s}_b^{11}-\mathbf{s}_t^{11}=\Delta\mathbf{a}_2, \quad \mathbf{F}_t^{11}+\mathbf{F}_b^{11}=\mathbf{0} \end{aligned} \tag{25}$$

where the superscripts refer to the RVE indexes, and the subscripts to the relevant segment of the RVE. We note that the equations on the right in (25) represent a weaker constraint than that in Eq. (14), since they do not enforce the equilibrium of the internal nodes. Now consider an RVE made of the union of the four RVEs (Fig. 4) under the same macroscopic deformation gradient. Also assume that no bifurcation point exists on the load path of the larger RVE from $\mathbf{0}$ to $\mathbf{G}$. Since all RVE^{ij} are identical, we can obtain a model of the assembly by static condensation starting from a model of the single unit. The static condensation equations for the RVEs are

$$\begin{aligned} &\mathbf{s}_r^{11}=\mathbf{s}_l^{12}, \quad \mathbf{F}_l^{11}+\mathbf{F}_r^{12}=\mathbf{0}\\ &\mathbf{s}_t^{12}=\mathbf{s}_b^{22}, \quad \mathbf{F}_t^{12}+\mathbf{F}_b^{22}=\mathbf{0}\\ &\mathbf{s}_l^{22}=\mathbf{s}_r^{21}, \quad \mathbf{F}_l^{22}+\mathbf{F}_r^{21}=\mathbf{0}\\ &\mathbf{s}_b^{21}=\mathbf{s}_t^{11}, \quad \mathbf{F}_t^{11}+\mathbf{F}_b^{11}=\mathbf{0} \end{aligned} \tag{26}$$

While the compatibility and the periodic equilibrium equations for the enlarged RVE, are

$$\begin{aligned} &\mathbf{s}_r^{11}-\mathbf{s}_l^{12}=2\Delta\mathbf{a}_1, \quad \mathbf{F}_l^{11}+\mathbf{F}_r^{12}=\mathbf{0}\\ &\mathbf{s}_r^{22}-\mathbf{s}_l^{21}=2\Delta\mathbf{a}_1, \quad \mathbf{F}_t^{21}+\mathbf{F}_b^{11}=\mathbf{0}\\ &\mathbf{s}_b^{11}-\mathbf{s}_t^{21}=2\Delta\mathbf{a}_2, \quad \mathbf{F}_l^{21}+\mathbf{F}_r^{22}=\mathbf{0}\\ &\mathbf{s}_b^{22}-\mathbf{s}_t^{12}=2\Delta\mathbf{a}_2, \quad \mathbf{F}_t^{22}+\mathbf{F}_b^{12}=\mathbf{0} \end{aligned} \tag{27}$$

As we can observe, since Eqs. (25) hold for each RVE^{ij}, Eqs. (26) and (27) are always satisfied, and the nodal configuration $\mathbf{s}^{11}=\mathbf{s}^{21}=\mathbf{s}^{12}=\mathbf{s}^{22}$ is a solution for the larger RVE under the macroscopic gradient $\mathbf{G}$. In other words, the periodic boundary conditions over a single RVE always satisfy static condensation equations and periodic boundary conditions if more RVEs are joined to build a larger one. Since no bifurcation point exists, this solution is unique. It follows that the predicted response of the material is not influenced by the RVE size. Therefore, the lattice equilibrium configuration before bifurcations is always periodic in the unit cell.

In the case that bifurcation points exist on the load path of the larger RVE, the equilibrium configuration is not unique. In this case, since conditions (27) are weaker than conditions (25), applied at each RVE^{ij}, it follows that solutions can exist that are compatible with the periodic equilibrium of the enlarged RVE, but do not satisfy the equilibrium conditions of the single RVE^{ij}. In particular, for these configurations Eq. (27) holds, but $\mathbf{s}^{11}\neq\mathbf{s}^{21}\neq\mathbf{s}^{12}\neq\mathbf{s}^{22}$. Therefore after bifurcation, each of the solutions that is periodic over a single RVE^{ij} is still solution of the enlarged RVE, and additional equilibrium configurations that are periodic only over the enlarged RVE exist. While each of these configurations is mathematically possible, only the one that minimises the total potential is a realistic configuration. If we consider RVEs with a larger number of unit cells, the set of possible buckled configurations enlarges, and can include more stable configurations. The choice of a larger RVE, however, would significantly increase the computational cost. Therefore, the RVE should be as small as possible to reduce the computational cost and be sufficiently large such that increasing its size would not significantly affect the predictions of the model. For a given lattice topology and values of the expected macroscopic deformations, an analysis should be carried out prior to selecting the size of the RVE with the goal of assessing the impact of the RVE size.

4. Effective properties of lattice materials

We now proceed to illustrate the predictions of the model for the effective properties of the lattices, made of a linear elastic solid material of Young's modulus E_s, under a range of applied boundary conditions. We note that in these examples, where we aim to investigate the effective properties, the stress and strain states of the lattices are macroscopically homogenous at the RVE scale. Thus, even though in the examples presented in this section we use the full solution procedure as described in Section 2 to illustrate and verify the method, simpler methods will suffice for the effective property calculation which only involves the analysis of a single RVE. Here we consider the hexagonal and the triangulated lattice that is typical examples of bending and stretching dominated topologies (Deshpande et al., 2001). These topologies are initially elastically isotropic and expressions of the lattice stiffness matrix, in terms of the Young's modulus of the solid material and the slenderness ratio are given as (Vigliotti and Pasini, 2012a)

$$\begin{bmatrix}\sigma_{11}\\ \sigma_{22}\\ \sigma_{12}\end{bmatrix}=\frac{E_s\lambda}{2\sqrt{3}(\lambda^2+1)}\begin{bmatrix}3\lambda^2+1 & 1-\lambda^2 & 0\\ 1-\lambda^2 & 3\lambda^2+1 & 0\\ 0 & 0 & 2\lambda^2\end{bmatrix}_{Hexa}=\begin{bmatrix}\varepsilon_{11}\\ \varepsilon_{22}\\ \varepsilon_{12}\end{bmatrix} \tag{28}$$

Please cite this article as: Vigliotti, A., et al., Non linear constitutive models for lattice materials. J. Mech. Phys. Solids (2013), http://dx.doi.org/10.1016/j.jmps.2013.10.015

$$\begin{bmatrix}\sigma_{11}\\ \sigma_{22}\\ \sigma_{12}\end{bmatrix} = \frac{E_s\lambda\sqrt{3}}{4}\begin{bmatrix}\lambda^2+3 & 1-\lambda^2 & 0\\ 1-\lambda^2 & \lambda^2+3 & 0\\ 0 & 0 & 2\lambda^2+1\end{bmatrix}_{Tria} = \begin{bmatrix}\varepsilon_{11}\\ \varepsilon_{22}\\ \varepsilon_{12}\end{bmatrix} \tag{29}$$

where σ_{ij} and ε_{ij} are the components of the macroscopic engineering stress and strain tensors, respectively, while the strut slenderness ratio $\lambda = t/L_0$, where t is the strut thickness, and L_0 is the strut length. From (28) and (29), expressions for the lattice bulk modulus, the Young's modulus, the Poisson ratio can be readily written as

$$K_{Hexa} = \frac{\lambda}{\sqrt{3}}E_s, \quad E_{Hexa} = \frac{4\lambda^3}{\sqrt{3}(3\lambda^2+1)}E_s, \quad \nu_{Hexa} = \frac{1-\lambda^2}{3\lambda^2+1} \tag{30}$$

$$K_{Tria} = \lambda\sqrt{3}E_s, \quad E_{Tria} = \frac{2\sqrt{3}\lambda(\lambda^2+1)}{\lambda^2+3}E_s, \quad \nu_{Tria} = \frac{1-\lambda^2}{3\lambda^2+3} \tag{31}$$

where $K_{...}$, $E_{...}$, and $\nu_{...}$ denote the bulk modulus, the Young's modulus, and Poisson ratio, respectively. The above equations include both bending and axial stretching contributions for the struts. Expressions valid for pin-jointed lattices, for which there are no bending contributions from the struts, can be obtained by neglecting the terms in λ^2 and higher order terms in Eqs. (28)–(31). We observe that the stiffness matrix of the pin-jointed hexagonal lattice is twice rank deficient and its Young's modulus is zero; nevertheless since the bulk modulus does not vanish, the pin-jointed lattice is still capable of withstanding hydrostatic macroscopic stress. This is caused by the bending dominated nature of the hexagonal lattice. On the other hand, the pin-jointed triangulated lattice responds to any macroscopic stresses with axial forces in the struts. We proceed to present results for the hexagonal and triangulated lattices that are characterised in terms of their relative density ρ^* (ratio of the density of the lattice to the density of the solid material from which the lattice is made). In terms of their slenderness ratio λ, the relative density of the hexagonal and triangulated lattices is $\rho^* = 2/\sqrt{3}\lambda$ and $\rho^* = 2\sqrt{3}\lambda$, respectively. Note that these formulae are accurate in the limit $\lambda \ll 1$, where we can neglect the volume of the nodes in comparison to the volumes of the struts. In this and in the following sections, we will keep fixed the slenderness ratio of the lattices struts to $\lambda = 1/50$. This corresponds to a relative density of $\rho^* = 0.02$ for the hexagonal lattice, and $\rho^* = 0.07$. Similar analyses can of course be conducted for arbitrary values of ρ^*.

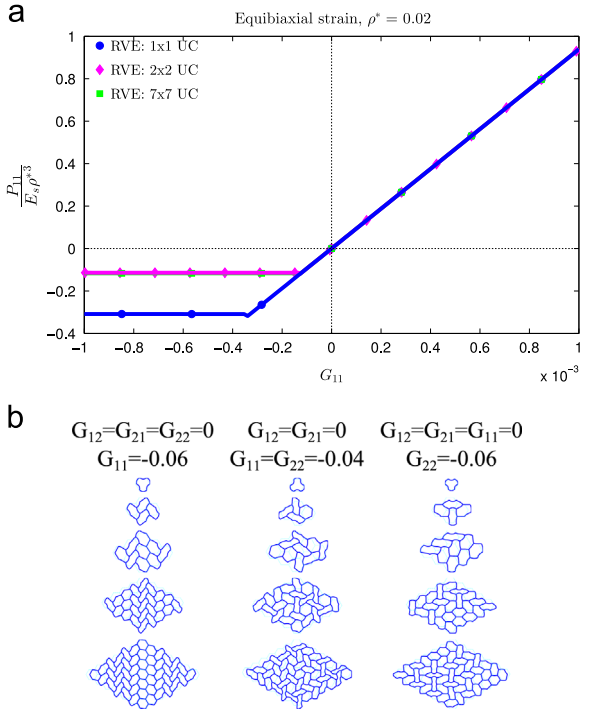

Fig. 5. (a) The predicted equi-biaxal normalised stress versus strain curve for the hexagonal lattice for selected choices of the RVE size. (b) The effect of RVE size on the predicted buckling modes three selected boundary conditions (uniaxial compressive straining in the 1 and 2-directions, and equi-biaxial compressive straining). The undeformed lattice is shown in cyan as a dotted line, while the deformed lattice is in blue solid line. (For interpretation of the references to colour in this figure caption, the reader is referred to the web version of this article.)

Please cite this article as: Vigliotti, A., et al., Non linear constitutive models for lattice materials. J. Mech. Phys. Solids (2013), http://dx.doi.org/10.1016/j.jmps.2013.10.015

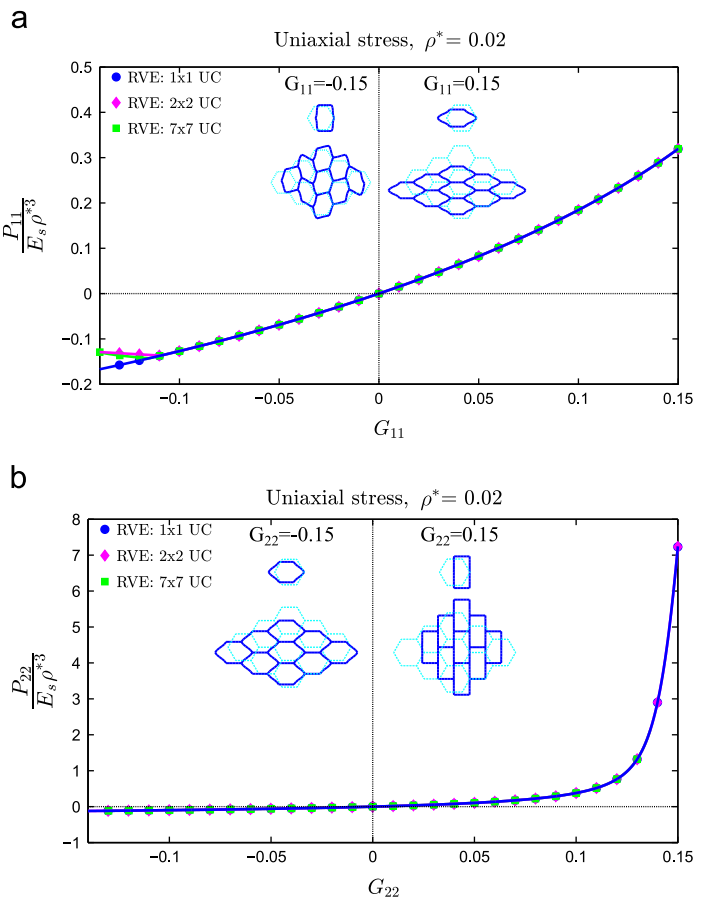

Fig. 6. The predicted uniaxial stressing responses of the hexagonal lattice in the (a) 1-direction and (b) 2-direction. Results are included for a range of RVE sizes while the deformed RVE shapes are shown for the 1×1 UC and 3×3 UC cases at selected values of the applied strains.

4.1. Hexagonal lattice

Eqs. (28) and (30) define the stiffness of the undeformed lattice. As the lattice deformation increases, the response deviates from the linear approximation, and different behaviours are possible depending on the applied boundary conditions. Let us first consider the response of the lattice subjected to an equi-biaxial straining. Fig. 5a shows the normalised stress $P_{22}/(E_s\rho^{*3})$ versus strain G_{22} curves obtained for equi-biaxial strain for three choices of RVE size. Numerical results for RVE size ranging between 2×2 UC and 7×7 UC are very similar to each other, and are not shown for conciseness. The boundary conditions applied to the material model are

$$G_{11} = G_{22}$$
$$G_{12} = G_{21} = 0 \tag{32}$$

where the components of G are with reference to the Cartesian co-ordinate system defined in Fig. 2. We recall from Gibson and Ashby (1999) that the buckling stress of the honeycomb is expected to scale as $E_s\rho^{*3}$ – hence we normalise the results in Fig. 5a, and the following figures, by using this factor. As expected, the curves in Fig. 5a overlap until they reach a bifurcation point on the load path. Because of the symmetry of the lattice, positive values of $G_{11} = G_{22}$ produce only axial tension forces on the struts; hence no bifurcation exists for tensile or positive strains. In contrast, a negative strain produces axial compression that induces buckling with a tangent stiffness that is nearly zero. We observe that the predicted critical load varies with the size of the RVE; in particular, the critical load, which corresponds to a RVE with a single UC, is substantially higher than the load predicted for larger RVEs. In addition, while the values of the buckling load for RVEs with more than one UC are quite close, no real trend exists as the RVE size increases.[2] We note that the main characteristic of the deformation mode under equi-biaixal compression is the lattice "folding" around a less-deformed hexagon. This deformation mechanism is in agreement with the results found by Papka and Kyriakides (1999) for equi-biaxial crushing

[2] The wavelength of buckling in our analysis is restricted to the RVE size. As finite deformations proceed, the natural buckling wavelengths may or may not exceed the preset RVE size and hence no definite trend in the collapse load with respect to the RVE size can be expected.

Please cite this article as: Vigliotti, A., et al., Non linear constitutive models for lattice materials. J. Mech. Phys. Solids (2013), http://dx.doi.org/10.1016/j.jmps.2013.10.015

of honeycombs. For these boundary conditions, the similarity of the buckling modes among RVEs with 2 or more UCs, suggests that the buckling of the hexagonal lattice has an effective wavelength of 2 unit cells. It is worth mentioning here that, prior to bifurcation, $P_{22}=P_{11}$; however, in post-bifurcation the two stresses are no longer equal as the equi-biaxial straining and stressing solutions diverge.

The buckling modes of the hexagonal lattice subjected to uniaxial compressive straining in the 1 and 2 -directions are illustrated in Fig. 5b. It is clear that similar to the equi-biaxial compression case, the deformation modes do not change significantly as the RVE size is increased beyond 2×2 UCs. From these observations, we conclude that the microscopic buckling of the hexagonal lattice is effectively governed by the modes with a wavelength of two UCs for a wide range of loading states and a 2×2 UC RVE should suffice to model the hexagonal lattice as a homogenised continuum. We note in passing that the buckling modes predicted here for uniaxial compressive straining (i.e. $G_{22}=0$ or $G_{11}=0$) are in agreement with the observations and predictions of Gibson and Ashby (1999).

We now proceed to examine the uniaxial stressing responses of the hexagonal lattice. First consider the case of uniaxial stressing in the 1-direction shown in Fig. 6a ($P_{22}=P_{12}=P_{21}=0$ with the applied loading applied by imposing a G_{11}). As for the case of biaxial straining (Fig. 5b), the predicted responses are independent of the RVE size prior to bifurcation. In fact, the applied boundary conditions prevent buckling to occur for the single UC RVE, which remains in the pre-buckling configuration with the anti-symmetric bending of the horizontal elements, as described by Zhang and Ashby (1992). The buckling of larger RVEs occurs at slightly different thresholds; nevertheless the buckling modes are all very similar (for the sake of brevity, the buckling modes only for 1×1 UC RVE and 3×3 UC RVE are shown in Fig. 5a). Next consider the case of uniaxial stressing in the 2-direction included in Fig. 6a ($P_{11}=P_{12}=P_{21}=0$ with the loading applied by imposing a G_{22}). Over the range of deformation considered here no buckling is predicted under both compressive and tensile loading, hence the responses are RVE-size independent.

4.2. Triangulated lattice

The results for the triangulated lattice are qualitatively similar to the hexagonal lattice; hence we only briefly discuss these, and focus on highlighting the differences between the hexagonal and triangulated lattices. The equi-biaxial straining response of the $\rho^*=0.07$ triangulated lattice is plotted in Fig. 7a for a selection of RVE sizes. Again, bifurcation occurs only in compression and the results are reasonably RVE-size independent for RVEs with 2×2 UCs or more. The buckling modes for three loading conditions (uniaxial compressive straining in the 1 and 2-directions and equi-biaxial compression) shown in Fig. 7b also confirm that an RVE with 2×2 UCs suffices to capture the buckling modes.

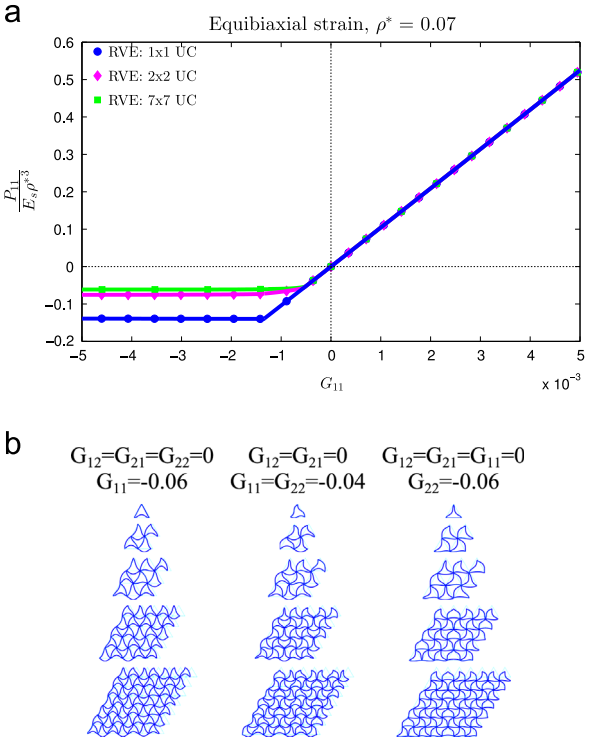

Fig. 7. (a) The predicted equi-biaxal normalised stress versus strain curve for the triangulated lattice for selected choices of the RVE size. (b) The effect of RVE size on the predicted buckling modes three selected boundary conditions (uniaxial compressive straining in the 1 and 2-directions and equi-biaxial compressive straining). The undeformed lattice is shown in cyan as a dotted line, while the deformed lattice is in blue solid line. (For interpretation of the references to colour in this figure caption, the reader is referred to the web version of this article.)

Please cite this article as: Vigliotti, A., et al., Non linear constitutive models for lattice materials. J. Mech. Phys. Solids (2013), http://dx.doi.org/10.1016/j.jmps.2013.10.015

The response of the triangulated lattice subjected to uniaxial stressing in the 1 and 2-directions is shown in Fig. 8a and b, respectively. We note that similar to the honeycomb, the triangulated lattice does not display a bifurcation under tensile loading in the 1-direction, but under compression the struts aligned with the loading direction buckle as shown in Fig. 8a. However, the stretching triangulated lattice induces compressive forces in the struts aligned in the 1-direction when subjected to uniaxial tensile loading in the 2-direction. Thus, under uniaxial stressing in the 2-direction, the response displays bifurcations under both compressive and tensile loadings although the bifurcation modes under compressive and tensile loadings differ, as shown in Fig. 8b.

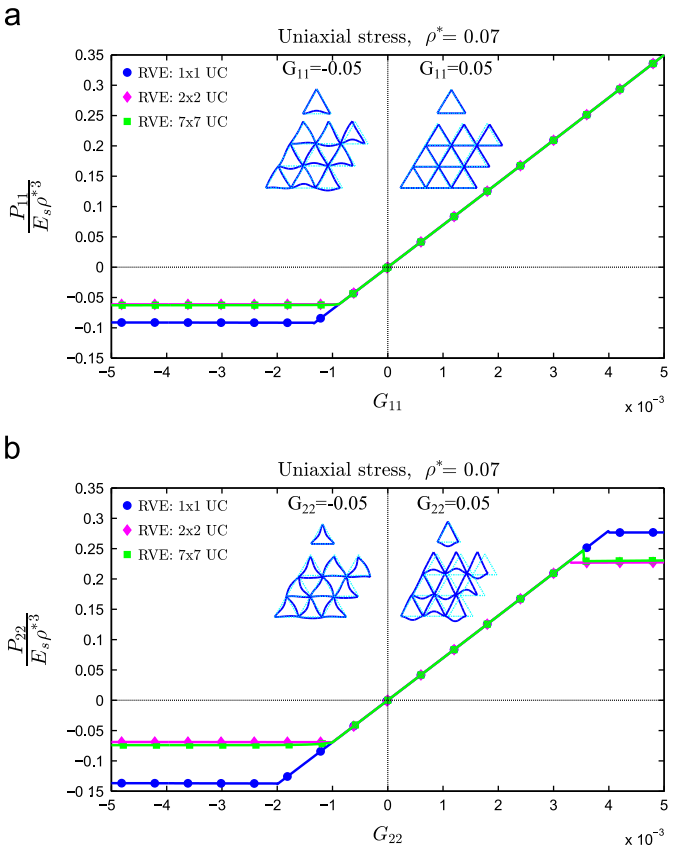

Fig. 8. The predicted uniaxial stressing responses of the triangulated lattice in the (a) 1-direction and (b) 2-direction. Results are included for a range of RVE sizes while the deformed RVE shapes are shown for the 1×1 UC and 3×3 UC cases at selected values of the applied strains.

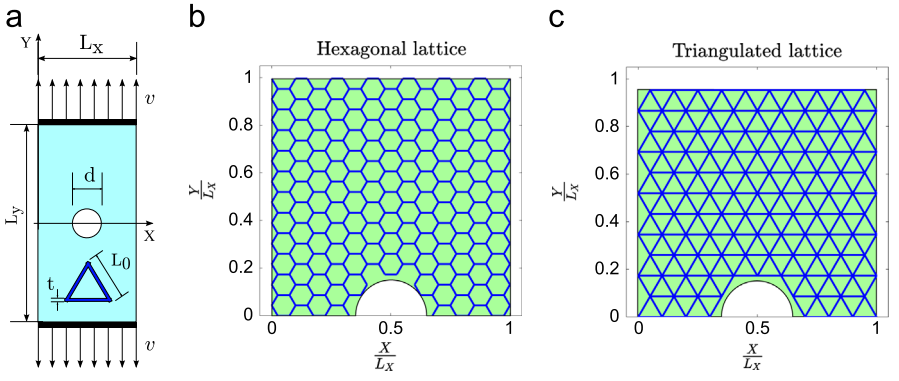

Fig. 9. (a) Sketch of the boundary value problem of the plate with a central circular hole. The global co-ordinate system is also indicated. Sketches of the (b) hexagonal and (c) triangulated lattices showing the orientation of the lattice with respect to the global co-ordinate system marked in (a) ($L_X/L_0 = 10$).

Please cite this article as: Vigliotti, A., et al., Non linear constitutive models for lattice materials. J. Mech. Phys. Solids (2013), http://dx.doi.org/10.1016/j.jmps.2013.10.015

5. Analysis of the uniaxial response of a lattice plate with a circular hole

The results in Section 4 describe the effective properties of the lattice materials subjected to large deformations. We now proceed to demonstrate the capabilities of the model by performing simulations of the uniaxial loading of a plate comprising either the hexagonal or triangulated lattice with a central circular hole. This problem generates a non-homogenous stress state within the plate, and the predictions of the homogenised model are compared with the predictions of a model wherein all the struts of the lattice within the domain are explicitly modelled.

The plate, with overall dimensions L_X and L_Y in the 1 and 2-directions respectively, and a central circular hole of diameter d, was subjected to remote tensile loading as shown in Fig. 9a. The orientations of the 2 lattices are sketched in Fig. 9b and c. The loading was applied to the top and bottom surfaces of the plate by applying a vertical displacement v as shown in Fig. 9, with the horizontal movements of all nodes on those surfaces completely constrained. For numerical convenience we only model its top half, i.e. a plate of dimensions L_X and $L_Y/2$, and impose symmetry boundary conditions along the $Y=0$ axis. We note that from symmetry, prior to bifurcations, this half-model is sufficient. However, bifurcations could break this

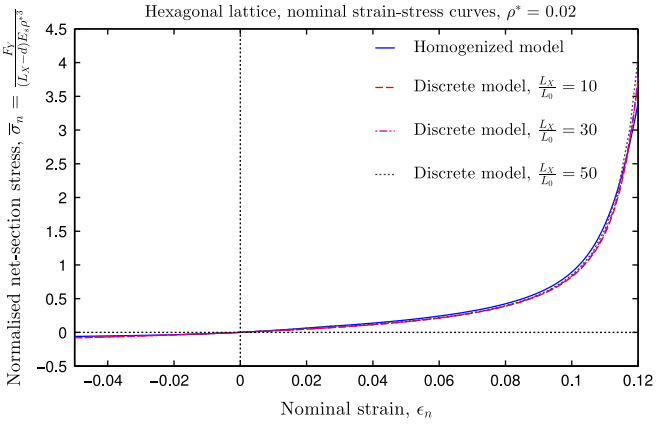

Fig. 10. Comparison between the predictions of the nominal stress versus strain response of the discrete and homogenised models for the uniaxial response of a plate made of the hexagonal lattice with a central circular hole. Predictions of the discrete model are shown for three choices of the normalised strut length L_X/L_0.

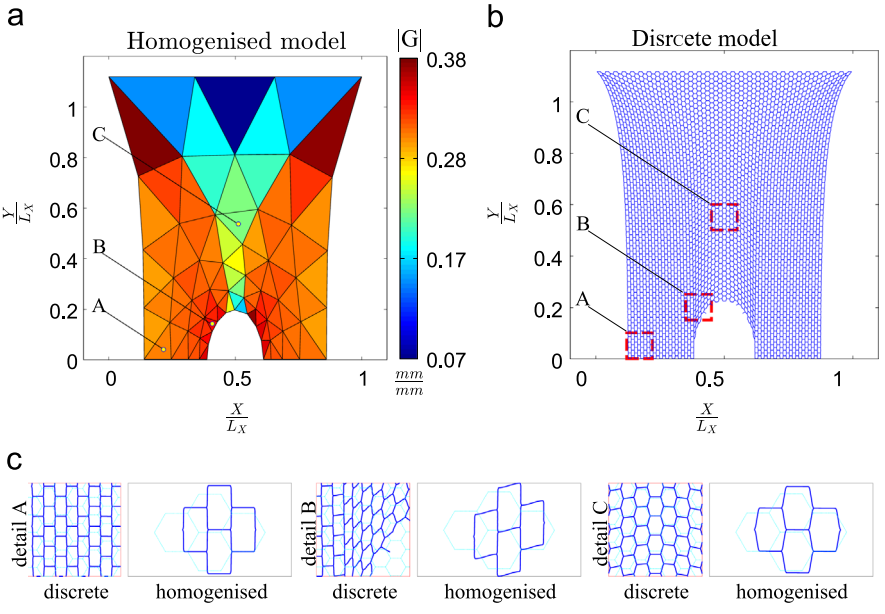

Fig. 11. The deformed configurations of the hexagonal lattice plate at an applied tensile strain $\varepsilon_n = 0.12$ using the (a) homogenised and (b) discrete ($L_X/L_0 = 30$) models. Contours of $|G|$ are included in (a). (c) A comparison between the predicted deformed cell shapes at three locations marked A, B and C. The undeformed lattice is shown in cyan as a dotted line, while the deformed lattice is in blue solid line. In each case the image on the left shows the deformed cells shapes as predicted by the discrete model while the image on the right is the RVE in the homogenised model. (For interpretation of the references to colour in this figure caption, the reader is referred to the web version of this article.)

Please cite this article as: Vigliotti, A., et al., Non linear constitutive models for lattice materials. J. Mech. Phys. Solids (2013), http://dx.doi.org/10.1016/j.jmps.2013.10.015

symmetry and the analysis presented here is restrictive in that sense. However, the aim here is to compare the predictions of the homogenised model with the predictions of a model wherein all the struts of the lattice within the domain are explicitly modelled and so long as the same boundary conditions are imposed in both models, the analysis is meaningful. In all the simulations presented here we kept $L_X/L_Y = 0.5$, $d/L_X = 0.3$ fixed. As in the previous section, we consider lattices with a strut aspect ratio $\lambda = 1/50$. In the homogenised model, the domain was discretised with plane, constant stress, triangular elements and the constitutive response assumed to be described by a 2×2 UC RVE. Each strut of the RVE was discretised by three Euler Bernoulli beams elements with cubic interpolation. The FE implementation of the homogenised model was carried out within an in-house code.

The discrete model, wherein each strut of the lattice is explicitly modelled, requires the specification of an additional length scale, viz. L_X/L_0 where L_0 is the length of the strut. Recall that the homogenised model implicitly assumes that L_X/L_0 tends to infinity as the constitutive model has no inherent length scale. In the discrete model L_X/L_0 varied from 10 to 50 in increments of 5 in order to probe for gauge the sensitivity of the response of the inherent length scale, thereby defining the regime of applicability of the homogenised model. These discrete simulations were conducted using the commercial FE package ABAQUS standard (version 6.10), where each strut is modelled as a Euler–Bernoulli beam (B23 in the ABAQUS notation).

We proceed to present results in terms of the net section nominal stress, which is the average of the stress on the symmetry line of the domain, $\sigma_n = F_Y/(L_Y - d)$ normalised by $E_s\rho^{*3}$ for uniformity with the data presented in Section 4, i.e. $\overline{\sigma}_n = \sigma_n/(E_s\rho^{*3})$. Here F_Y is force conjugate to the applied displacements v versus the nominal strain $\varepsilon_n = 2v/L_Y$.

5.1. Hexagonal lattice

Predictions of $\overline{\sigma}_n$ versus ε_n for the discrete and homogenised models are included in Fig. 10 for compressive and tensile loading. For brevity we only show curves for three selected values of L_X/L_0. Similar to the effective properties discussed in Section 4, no bifurcations under both uniaxial compressive and tensile loading are observed even for a plate with a central circular hole. The homogenised model is in excellent agreement with the predictions of the discrete model for plates with more than 10 cells across the plate width. In fact, the predictions of the discrete model are reasonably insensitive to L_X/L_0 for $L_X/L_0 > 10$.

The homogenised model captures the features of the response of the plate under compressive and tensile loading with a high level of accuracy. Under compressive loading the lattice deforms by bending of the cells walls at low nominal compressive stresses. However, under tensile loading the cells walls tend to align with the loading, which results in the stiffening of the curve, as seen in Fig. 10. To further investigate this, we proceed to compare the deformation modes as predicted by the discrete and homogenised models. The discrete results are presented for the choice $L_X/L_0 = 30$, but it is worth recalling that the predictions are reasonably insensitive to this choice of length scale. The deformed configurations of

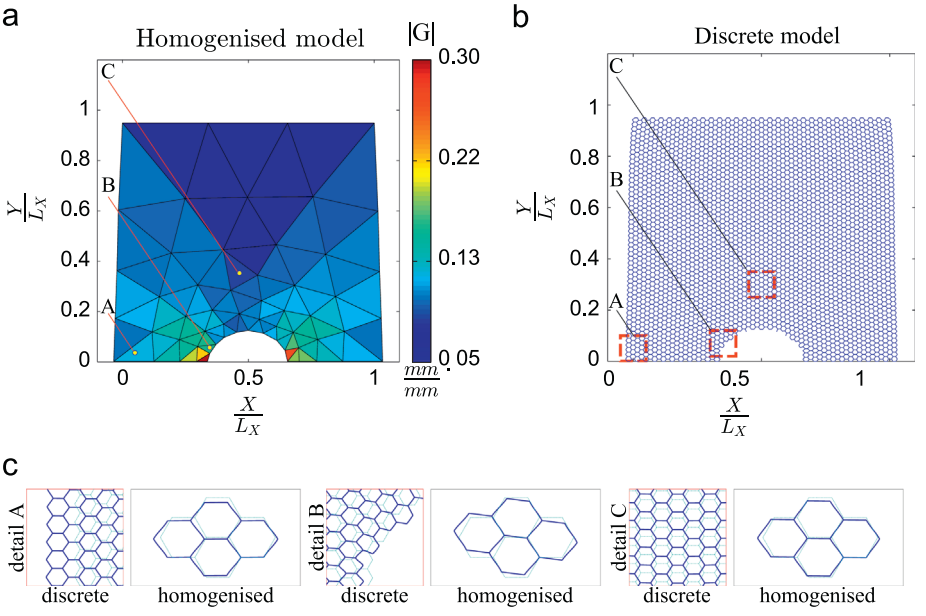

Fig. 12. The deformed configurations of the hexagonal lattice plate at an applied compressive strain $\varepsilon_n = -0.048$ using the (a) homogenised and (b) discrete ($L_X/L_0 = 30$) models. Contours of $|G|$ are included in (a). (c) A comparison between the predicted deformed cell shapes at three locations marked A, B and C. The undeformed lattice is shown in cyan as a dotted line, while the deformed lattice is in blue solid line. In each case the image on the left shows the deformed cells shapes as predicted by the discrete model while the image on the right is the RVE in the homogenised model. (For interpretation of the references to colour in this figure caption, the reader is referred to the web version of this article.)

Please cite this article as: Vigliotti, A., et al., Non linear constitutive models for lattice materials. J. Mech. Phys. Solids (2013), http://dx.doi.org/10.1016/j.jmps.2013.10.015

the plate at an applied strain $\varepsilon_n = 0.12$ are shown in Fig. 11a and b for the homogenised and discrete models. The mesh used on the homogenised analysis is depicted in Fig. 11a and shaded with contours of the norm of the deformation gradient $|G| = \sqrt{G_{ij}G_{ij}}$. The overall deformed shapes of the plate and hole are in excellent agreement between the homogenised and discrete models. To further investigate the fidelity of the homogenised model, we proceed to compare the deformed lattices at three representative locations in the plate marked in Fig. 11a and b. Locations A and C are located away from the hole and excellent agreement is seen in Fig. 11c between the deformed shapes of the cells as predicted by the discrete and homogenised models (approximately 8×5 cells are shown for the discrete model at each of these locations, while the 2×2 UC RVE is shown for the homogenised model). Both the models predict that the cells of the hexagonal lattice deform such that some cell walls align with the loading direction. At location B, which is at the edge of the hole, the discrete model predicts a large gradient in the pattern of the cells deformation. While 2 layers of cells at the edge of the hole undergo large shearing deformations, the lattice deformation at location B is similar to that at location A for cells that are more than 2 strut

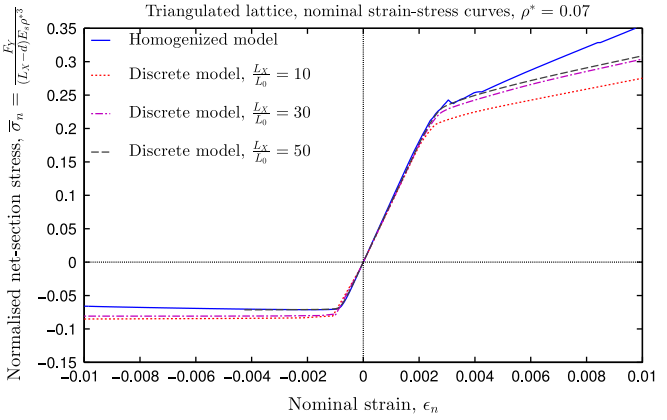

Fig. 13. Comparison between the predictions of the nominal stress versus strain response of the discrete and homogenised models for the uniaxial response of a plate made of the triangulated lattice with a central circular hole. Predictions of the discrete model are shown for three choices of the normalised strut length L_X/L_0.

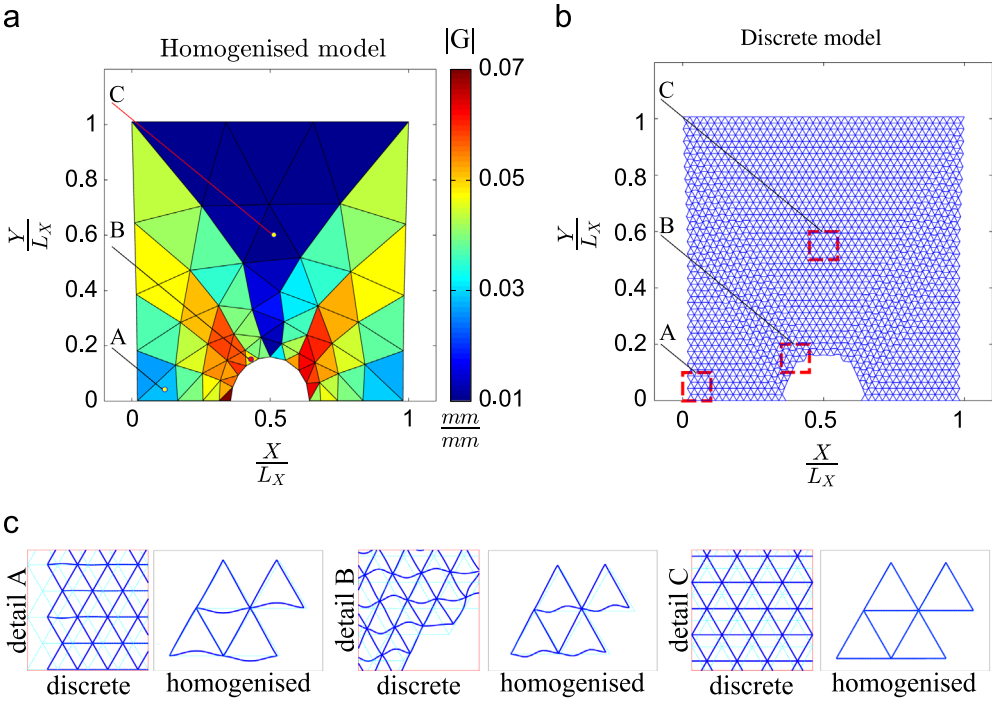

Fig. 14. The deformed configurations of the triangulated lattice plate at an applied tensile strain $\varepsilon_n = 0.01$ using the (a) homogenised and (b) discrete ($L_X/L_0 = 30$) models. Contours of $|G|$ are included in (a). (c) A comparison between the predicted deformed cell shapes at three locations marked A, B and C. The undeformed lattice is shown in cyan as a dotted line, while the deformed lattice is in blue solid line. In each case the image on the left shows the deformed cells shapes as predicted by the discrete model while the image on the right is the RVE in the homogenised model. (For interpretation of the references to colour in this figure caption, the reader is referred to the web version of this article.)

Please cite this article as: Vigliotti, A., et al., Non linear constitutive models for lattice materials. J. Mech. Phys. Solids (2013), http://dx.doi.org/10.1016/j.jmps.2013.10.015

lengths away from the hole. The homogenised model of course is unable to predict these variations that typically occur on the length scale of a single cell, but captures the general pattern of deformation a few cells away from the hole edge. The equivalent comparisons for compressive loading at an applied strain $\varepsilon_n = -0.048$ are shown in Fig. 12 with similar conclusions.

5.2. Triangulated lattice

Predictions of $\overline{\sigma}_n$ versus ε_n for the discrete and homogenised models are illustrated in Fig. 13 for compressive and tensile loading. There are some key differences with the hexagonal lattice case:

(i) In line with the effective properties discussed in Section 4, bifurcations are observed under both tensile and compressive loadings of the plate with a circular hole. The bifurcations under compressive loading are seen to result in a slightly negative tangent stiffness suggesting a loss of ellipticity of the overall governing equations of the homogenised model (Needleman, 1988). While a strongly softening material response gives rise to a large mesh sensitivity in the results, this mild softening observed here is found not to result in significant mesh dependence in the results reported in this work.
(ii) While the discrete and homogenised models are in excellent agreement prior to bifurcation, the homogenised model differs from the discrete results for values of $L_X/L_0 < 30$. The differences are larger under tensile loading where the homogenised model over predicts the discrete results. However, as anticipated, the discrete and homogenised predictions tend to converge as $L_X/L_0 \to \infty$.

We also observe that the predicted buckling stress is in good agreement with the results of Fig. 8b for RVEs of the triangulated lattice under uniaxial stressing in direction 2, both in tension and in compression. We remark that the data shown in Fig. 13, refer to the symmetry line of the domain at $Y=0$. Here the local stress is higher because of section reduction due to the presence of the hole; it follows that the buckling of the lattice struts initiate in this region as shown in detail in Figs. 14 and 15.

We proceed to compare the deformation modes in the discrete and homogenised models to understand the source of the discrepancy observed in the tensile branch of the plot in Fig. 13. Similar to Fig. 11, Fig. 14 shows a comparison between the homogenised and discrete models for the triangulated lattice plate subjected to a nominal tensile strain of $\varepsilon_n = 0.01$. At locations A and C, the deformation modes as predicted by the discrete and homogeneous models are in good agreement but

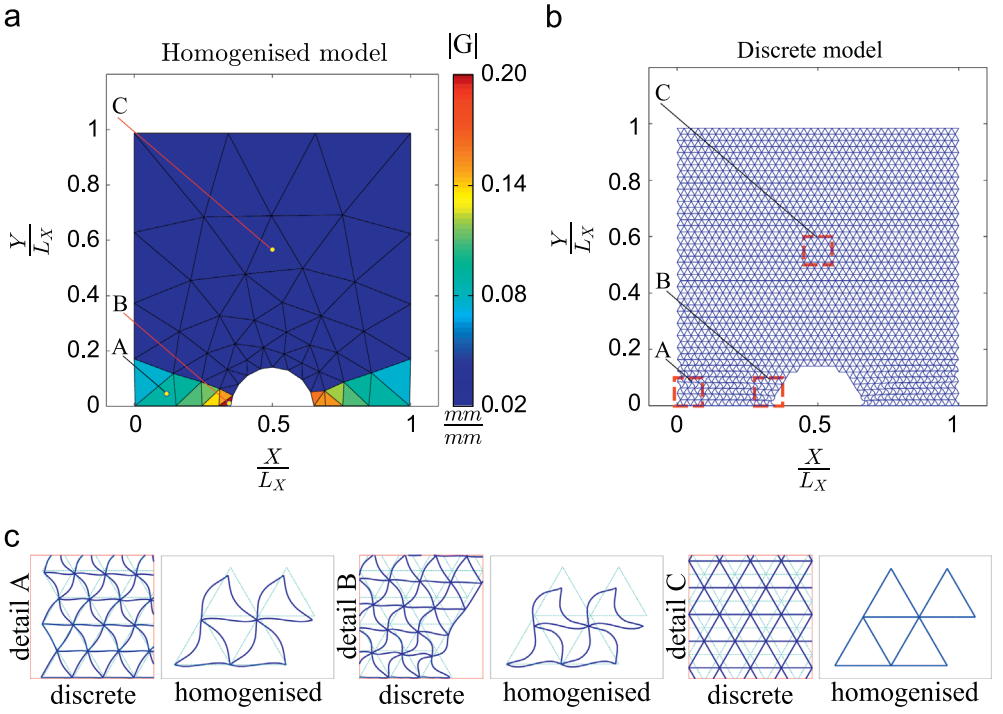

Fig. 15. The deformed configurations of the hexagonal lattice plate at an applied compressive strain $\varepsilon_n = -0.01$ using the (a) homogenised and (b) discrete ($L_X/L_0 = 30$) models. Contours of $|G|$ are included in (a). (c) A comparison between the predicted deformed cell shapes at three locations marked A, B and C. The undeformed lattice is shown in cyan as a dotted line, while the deformed lattice is in blue solid line. In each case the image on the left shows the deformed cells shapes as predicted by the discrete model while the image on the right is the RVE in the homogenised model. (For interpretation of the references to colour in this figure caption, the reader is referred to the web version of this article.)

Please cite this article as: Vigliotti, A., et al., Non linear constitutive models for lattice materials. J. Mech. Phys. Solids (2013), http://dx.doi.org/10.1016/j.jmps.2013.10.015

at the edge of the hole, i.e. location B, the homogeneous model predicts buckling of the horizontal struts in the higher order mode compared to the discrete model. We expect that it is this discrepancy between the homogenised and discrete models that result in the homogenised model overpredicting the discrete results in the tensile regime.

Similar comparisons between the deformation mode predictions of the discrete and homogenised models for an applied compressive strain $\varepsilon_n = -0.01$ are included in Fig. 15. In line with the excellent agreement between the compressive stress versus strain predictions seen in Fig. 13, the deformation modes of the homogenised and discrete ($L_X/L_0 = 30$) are in good agreement at the locations A, B and C in Fig. 15.

We emphasise here that unlike the hexagonal lattice, the triangulated lattice displays bifurcations under both compressive and tensile loadings. Thus, the predictions of the homogenised model are expected to be sensitive to the choice of the RVE: the 2×2 UC RVE selected here is shown to give predictions of sufficient fidelity.

6. Conclusions

The paper has presented a methodology for the numerical evaluation of the constitutive law of lattice materials. The approach is based on numerical homogenisation and can account for the non linear behaviours of lattices with arbitrary topology. The hexagonal and the triangulated lattices have been selected as case studies and have been analysed in detail. The influence of the size of the representative volume element (RVE) on the predicted lattice behaviour has been discussed.

We have shown that if no bifurcation point is reached on the load path of the lattice, the predictions of the homogenised model are independent of the size of the RVE. On the other hand in the presence of bifurcations, the choice of the RVE influences the behaviour of the material model and a detailed analysis should be performed to select the appropriate RVE size of the continuous model. In particular, for the lattices under investigation, a single Unit Cell (UC) RVE provides a higher estimate of the strength, whereas RVEs including two or more UC yield similar values.

The method has then been applied to analyse a rectangular domain with a central hole made of a lattice material, under in plane compressive and tensile loads. The results from the discrete models have been compared to the prediction of the continuous models. We have found a good qualitative and quantitative agreement among the models. The homogenised model of the hexagonal lattice could capture its typical compliant behaviour in compression, and the stiffening effect due to the reorientation of the struts along the load direction in tension. With reference to the triangulated lattice, the homogenised model could also describe the buckling of the struts for both macroscopic compression and tension. Since a bifurcation occurs in the response of the triangulated lattice it follows that the predictions of the homogenised model are sensitive to the choice of the RVE. For the 2×2 UC chosen in the calculations presented here, the results of the homogenised and discrete models are in reasonable agreement.

References

Ashby, M.F., 2005. Materials Selection in Mechanical Design. Elsevier.
Banhart, J., 2001. Manufacture, characterisation and application of cellular metals and metal foams. Progr. Mater. Sci. 46 (6), 559-U3.
Bidanda, B., Bartolo, P., 2008. Virtual Prototyping & Bio Manufacturing in Medical Applications. Springer, US.
Braides, A., 1985. Homogenization of some almost periodic coercive functional. Rend. Accad. Naz. Sci. XL Mem. Mat. 5 (9), 313–321.
Charalambakis, N., 2010. Homogenization techniques and micromechanics. A survey and perspectives. Appl. Mech. Rev. 63 (3), 1–10.
Crisfield, M.A., 1981. A fast incremental-iterative solution procedure that handles snap-through. Comput. Struct. 13 (1–3), 55–62.
Crisfield, M.A., 1998. Non-Linear Finite Element Analysis of Solids and Structures, vol. 2. Wiley.
Deshpande, V.S., Ashby, M.F., Fleck, N.A., 2001. Foam topology: bending versus stretching dominated architectures. Acta Mater. 49 (6), 1035–1040.
Elsayed, M.S.A., Pasini, D., 2010a. Analysis of the elastostatic specific stiffness of 2D stretching-dominated lattice materials. Mech. Mater. 42 (7), 709–725.
Elsayed, M.S.A., Pasini, D., 2010b. Multiscale structural design of columns made of regular octet-truss lattice material. Int. J. Solids Struct. 47 (14–15), 1764–1774.
Eshelby, J.D., 1957. The determination of the elastic field of an ellipsoidal inclusion, and related problems. Proc. R. Soc. Lond. Ser. A: Math. Phys. Sci. 241 (1226), 376–396.
Fish, J., Wagiman, A., 1993. Multiscale finite element method for a locally nonperiodic heterogeneous medium. Comput. Mech. 12 (3), 164–180.
Fleck, N.A., Deshpande, V.S., Ashby, M.F., 2010. Micro-architectured materials: past, present and future. Proc. R. Soc. A: Math. Phys. Eng. Sci. 466 (2121), 2495–2516.
Gibson, L.J., Ashby, M.F., 1982. The mechanics of 3-dimensional cellular materials. Proc. R. Soc. Lond. Ser. A: Math. Phys. Eng. Sci. 382 (1782), 43.
Gibson, L.J., Ashby, M.F., 1999. Cellular Solids: Structure and Properties. Cambridge University Press.
Gibson, L.J., Ashby, M.F., Schajer, G.S., Robertson, C.I., 1982. The mechanics of two-dimensional cellular materials. Proc. R. Soc. Lond. Ser. A: Math. Phys. Eng. Sci. 382 (1782), 25–42.
Gitman, I.M., Askes, H., Sluys, L.J., 2007. Representative volume: existence and size determination. Eng. Fract. Mech. 74 (16), 2518–2534.
Gonella, S., Ruzzene, M., 2008. Homogenization and equivalent in-plane properties of two-dimensional periodic lattices. Int. J. Solids Struct. 45 (10), 2897–2915.
Gong, L., Kyriakides, S., Triantafyllidis, N., 2005. On the stability of kelvin cell foams under compressive loads. J. Mech. Phys. Solids 53 (4), 771–794.
Graham, S., Yang, N., 2003. Representative volumes of materials based on microstructural statistics. Scripta Mater. 48 (3), 269–274.
Gusev, A.A., 1997. Representative volume element size for elastic composites: a numerical study. J. Mech. Phys. Solids 45 (9), 1449–1459.
Hutchinson, R.G., Fleck, N.A., 2006. The structural performance of the periodic truss. J. Mech. Phys. Solids 54 (4), 756–782.
Kanit, T., Forest, S., Galliet, I., Mounoury, V., Jeulin, D., 2003. Determination of the size of the representative volume element for random composites: statistical and numerical approach. Int. J. Solids Struct. 40 (13–14), 3647–3679.
Kouznetsova, V., Brekelmans, W.A.M., Baaijens, F.P.T., 2001. An approach to micro-macro modeling of heterogeneous materials. Comput. Mech. 27 (1), 37–48.
Kouznetsova, V., Geers, M.G.D., Brekelmans, W.A.M., 2002. Multi-scale constitutive modelling of heterogeneous materials with a gradient-enhanced computational homogenization scheme. Int. J. Numer. Methods Eng. 54 (8), 1235–1260.

Please cite this article as: Vigliotti, A., et al., Non linear constitutive models for lattice materials. J. Mech. Phys. Solids (2013), http://dx.doi.org/10.1016/j.jmps.2013.10.015

Kouznetsova, V.G., Geers, M.G.D., Brekelmans, W.A.M., 2004. Multi-scale second-order computational homogenization of multi-phase materials: a nested finite element solution strategy. Comput. Methods Appl. Mech. Eng. 193 (48–51), 5525–5550.
Kumar, R.S., McDowell, D.L., 2004. Generalized continuum modeling of 2-D periodic cellular solids. Int. J. Solids Struct. 41 (26), 7399–7422.
Langley, R.S., 1996. The response of two-dimensional periodic structures to point harmonic forcing. J. Sound Vibrat. 197 (4), 447–469.
Matsui, K., Terada, K., Yuge, K., 2004. Two-scale finite element analysis of heterogeneous solids with periodic microstructures. Comput. Struct. 82 (7–8), 593–606.
Mohr, D., 2005. Mechanism-based multi-surface plasticity model for ideal truss lattice materials. Int. J. Solids Struct. 42 (11–12), 3235–3260.
Müller, S., 1987. Homogenization of nonconvex integral functionals and cellular elastic materials. Arch. Rational Mech. Anal. 99 (3), 189–212.
Needleman, A., 1988. Material rate dependence and mesh sensitivity in localization problems. Comput. Meth. Appl. Mech. Eng. 67 (1), 69–85.
Ohno, N., Okumura, D., Noguchi, H., 2002. Microscopic symmetric bifurcation condition of cellular solids based on a homogenization theory of finite deformation. J. Mech. Phys. Solids 50 (5), 1125–1153.
Papka, S.D., Kyriakides, S., 1999. In-plane biaxial crushing of honeycombs—Part II: analysis. Int. J. Solids Struct. 36 (29), 4397–4423.
Pindera, M.J., Khatam, H., Drago, A.S., Bansal, Y., 2009. Micromechanics of spatially uniform heterogeneous media: a critical review and emerging approaches. Composites B: Eng. 40 (5), 349–378.
Ramirez, D.A., Murr, L.E., Li, S.J., Tian, Y.X., Martinez, E., Martinez, J.L., Machado, B.I., Gaytan, S.M., Medina, F., Wicker, R.B., 2011. Open-cellular copper structures fabricated by additive manufacturing using electron beam melting. Mater. Sci. Eng.: A 528 (16–17), 5379–5386.
Schaedler, T.A., Jacobsen, A.J., Torrents, A., Sorensen, A.E., Lian, J., Greer, J.R., Valdevit, L., Carter, W.B., 2011. Ultralight metallic microlattices. Science 334 (6058), 962–965.
Smit, R.J.M., Brekelmans, W.A.M., Meijer, H.E.H., 1998. Prediction of the mechanical behavior of nonlinear heterogeneous systems by multi-level finite element modeling. Comput. Methods Appl. Mech. Eng. 155 (1–2), 181–192.
Spadoni, A., Ruzzene, M., 2007. Static aeroelastic response of chiral-core airfoils. J. Intell. Mater. Syst. Struct. 18 (10), 1067–1075.
Stroeven, M., Askes, H., Sluys, L.J., 2004. Numerical determination of representative volumes for granular materials. Comput. Methods Appl. Mech. Eng. 193 (30–32), 3221–3238.
Suiker, A.S.J., Metrikine, A.V., de Borst, R., 2001. Comparison of wave propagation characteristics of the Cosserat continuum model and corresponding discrete lattice models. Int. J. Solids Struct. 38 (9), 1563–1583.
Terada, K., Hori, M., Kyoya, T., Kikuchi, N., 2000. Simulation of the multi-scale convergence in computational homogenization approaches. Int. J. Solids Struct. 37 (16), 2285–2311.
Triantafyllidis, N., Schraad, M., 1998. Onset of failure in aluminum honeycombs under general in-plane loading. J. Mech. Phys. Solids 46 (6), 1089–1124.
Van Der Sluis, O., Schreurs, P.J.G., Brekelmans, W.A.M., Meijer, H.E.H., 2000. Overall behaviour of heterogeneous elastoviscoplastic materials: effect of microstructural modelling. Mech. Mater. 32 (8), 449–462.
Vigliotti, A., Pasini, D., 2012a. Linear multiscale analysis and finite element validation of stretching and bending dominated lattice materials. Mech. Mater. 46, 57–68.
Vigliotti, A., Pasini, D., 2012b. Stiffness and strength of tridimensional periodic lattices. Comput. Methods Appl. Mech. Eng..
Wang, A.J., McDowell, D.L., 2004. In-plane stiffness and yield strength of periodic metal honeycombs. J. Eng. Mater. Technol. Trans. ASME 126 (2), 137–156.
Wang, J., Nausieda, A., Lucato, S.L.D.E., Evans, A.G., 2007. Twisting of a high authority morphing structure. Int. J. Solids Struct. 44 (9), 3076–3099.
Zhang, J., Ashby, M.F., 1992. Buckling of honeycombs under inplane biaxial stresses. Int. J. Mech. Sci. 34 (6), 491.
Zhu, H.X., Knott, J.F., Mills, N.J., 1997. Analysis of the elastic properties of open-cell foams with tetrakaidecahedral cells. J. Mech. Phys. Solids 45 (3), 319.

Please cite this article as: Vigliotti, A., et al., Non linear constitutive models for lattice materials. J. Mech. Phys. Solids (2013), http://dx.doi.org/10.1016/j.jmps.2013.10.015